School of Mathematical
and Physical Sciences

University of

Department of Mathematics and Statistics

Preprint MPS-2011-03

28 March 2011

A moving mesh approach for modelling avascular tumour growth

by

familiar from Lagrangian fluid dynamics, and their numerical application to PDEs can be found for example in the Moving Finite Element method [4], the Deformation method [5], the GCL

focus on a two-phase model to clearly demonstrate the velocity-based moving mesh schemes, which can be adapted to numerically solve more sophisticated models.

In the next section we present the normalised one-dimensional model proposed in [1], followed by §3 where we surmise the fixed numerical mesh method used in [1], so as to compare results with the three moving mesh strategies. The details of these strategies are given in §4, where we solve the tumour growth model numerically using each one in turn. The results from the fixed mesh method and the three moving mesh methods are discussed in §5. Finally, in §6 we conclude that a moving mesh method can prove to be an elegant and accurate numerical approach that updates the mesh smoothly with the solution of the orginal model, whilst preserving chosen features of the model such as local mass balance, or relative partial masses, (for self-similar problems, similarity can be preserved). However, since the mesh depends upon the model, care must be taken when choosing a feature of the model to preserve.

2. A mathematical model of tumour growth

The model assumes the tumour consists of two phases, water and live cells, which are treated as incompressible fluids whose densities are equal, to leading order. The model is derived by applying mass balance to the cell and water phases. Further assumptions made are that inertial effects are negligible, no external forces act on the system, and, on the timescale of interest, the cell and water phases can be treated as viscous and inviscid fl

In the next three sections we show that moving the mesh to preserve features of the model can produce results in line with [1]. We also present results which demonstrate that the local feature of the model used to track the nodes needs to be carefully chosen.

3. Rescaling to a fixed numerical mesh

In [1] the moving domain $x \in [0, \ell(t)]$ is mapped to a fixed numerical domain $\xi \in [0, 1]$ by the transformation $\xi = x/\ell(t)$, $\tau = t$. Using the chain rule to differentiate $\alpha(\xi, \tau)$ with respect to time τ, the transformed problem is

$$\frac{\partial \alpha}{\partial \tau} - \frac{\xi}{\ell}\frac{d\ell}{d\tau}\frac{\partial \alpha}{\partial \xi} + \frac{1}{\ell}\frac{\partial}{\partial \xi}(u_c \alpha) = S(\alpha, C), \tag{8}$$

$$\frac{\partial}{\partial \xi}\left[\mu\alpha\frac{\partial u_c}{\partial \xi} - \ell\alpha\frac{\alpha - \alpha^*}{(1-\alpha)^2}H(\alpha - \alpha_{\min})\right] = \frac{k\ell^2\alpha u_c}{1-\alpha}, \tag{9}$$

$$\frac{\partial^2 C}{\partial \xi^2} = \frac{Q\ell^2\alpha C}{1 + \hat{Q}_1 C}, \tag{10}$$

with initial and boundary conditions

$$\ell = 1, \quad \alpha = \alpha^0 \qquad \alpha)$$

Step F2: Find u_j^m by applying central finite differences to (9),

$$\frac{1}{\Delta\xi}\left[\alpha^m_{j+\frac{1}{2}}\left[\mu\frac{u^m_{j+1}-u^m_j}{\Delta\xi}-\square^m\frac{\alpha^m_{j+\frac{1}{2}}-\alpha^*}{(1-\alpha^m_{j+\frac{1}{2}})^2}\mathrm{H}(\alpha^m_{j+\frac{1}{2}}-\alpha_{\min})\right]\right.$$
$$\left.-\alpha^m_{j-\frac{1}{2}}\left[\mu\frac{u^m_j-u^m_{j-1}}{\Delta\xi}-\square^m\frac{\alpha^m_{j-\frac{1}{2}}-\alpha^*}{(1-\alpha^m_{j-\frac{1}{2}})^2}\mathrm{H}(\alpha^m_{j-\frac{1}{2}}-\alpha_{\min})\right]\right]=\frac{k(\square^m)^2\alpha^m_j}{1-\alpha^m_j}u^m_j,\quad(15)$$

for $j = 1, 2, \ldots, N-1$, where $\alpha^m_{j+\frac{1}{2}} = \frac{1}{2}(\alpha^m_j + \alpha^m_{j+1})$ and $\alpha^m_{j-\frac{1}{2}} = \frac{1}{2}(\alpha^m_{j-1} + \alpha^m_j)$, leading to a linear system of equations. At the inner boundary $u^m_0 = 0$, as given by (12). To determine u^m_N, we discretise the boundary condition (13) by taking values $[\cdot]^m_{N-\frac{1}{2}}$ and $[\cdot]^m_{N+\frac{1}{2}}$ (the average about $[\cdot]^m_N$) to obtain

$$\frac{1}{2}\left[\mu\frac{u^m_{N+1}-u^m_N}{\Delta\xi}-\square^m\frac{\alpha^m_{N+\frac{1}{2}}-\alpha^*}{}\right.$$

This velocity-based strategy is similar to the numerical mapping in §

The updated total mass $\theta^{m+1} \approx \theta(t^{m+1})$ is then found using (31) and the same time-stepping approach used in Step 4, i.e. $\theta^{m+1} = \theta^m + \Delta t \dot{\theta}^m$.

To derive an expression for the mesh velocity, we again use Leibnitz' integral rule on (29) to calculate

$$\gamma_j \dot{\theta}(t) = \frac{\mathrm{d}}{\mathrm{d}t} \int_0^{\tilde{x}_j(t)} \alpha)$$

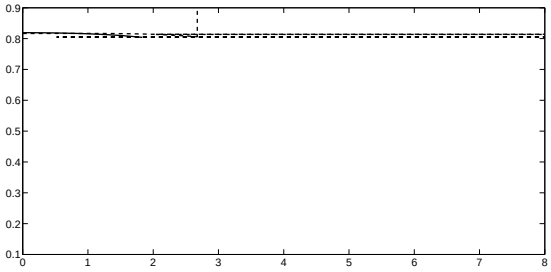
0.9
0.8
0.7
0.6
0.5
0.4
0.3
0.2
0.1
0
1
2
3
4
5
6
7
8

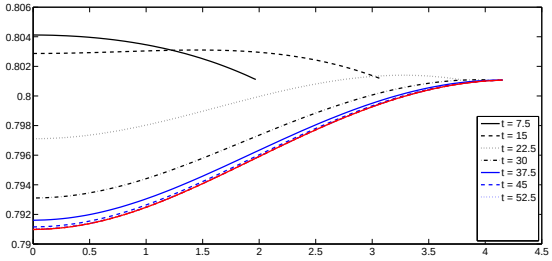
0.806
0.804
0.802
0.8
0.798
0.796
0.794
0.792
0.79
0
0.5
1
1.5
2
2.5
3
3.5
4
4.5
t = 7.5
t = 15
t = 22.5
t = 30
t = 37.5
t = 45
t = 52.5

Since each step of our scheme is second order in space and first order in time, and recalling that $\Delta t = O\left(\frac{1}{N^2}\right)$, we might expect to see $p, q \approx 2$, although since our meshes are generally non-uniform and varying in time, this is only an approximate hypothesis. Convergence results are

Method	N	$E_N(\alpha)$	p_{2N}	$E_N(\tilde{x})$	q_{2N}
A	10	2.034×10^{-4}	-	1.275×10^{-5}	-
	20	8.346×10^{-5}	1.3	3.306×10^{-6}	1.9
	40	3.547×10^{-5}	1.2	8.478×10^{-7}	2.0
	80	1.471×10^{-5}	1.3	2.050×10^{-7}	2.0
B	10	2.299×10^{-4}	-	6.207×10^{-4}	-
	20	9.293×10^{-5}	1.3	1.109×10^{-4}	2.5
	40	3.891×10^{-5}	1.3	3.043×10^{-5}	1.9
	80	1.600×10^{-5}	1.3	7.224×10^{-6}	2.1
C	10	1.448×10^{-5}	-	1.819×10^{-5}	-
	20	3.645×10^{-6}	2.0	1.944×10^{-6}	3.2
	40	8.807×10^{-7}	2.0	7.148×10^{-7}	1.5
	80	2.090×10^{-7}	2.1	1.880×10^{-7}	1.9

Table 1: Relative errors for α and $\tilde{x}$ with rates of convergence using the explicit Euler time-stepping scheme.

shown in Table 1. We see that $E_N(\alpha)$ and $E_N(\tilde{x})$ decrease as N increases for each of the moving mesh methods. This strongly suggests that as the number of nodes increases, both the solution α and the position of the nodes $\tilde{x}_j$ are converging. For Methods A and B, the p-values presented in this table indicate superlinear convergence of α, and the q-values suggest second-order convergence of $\tilde{x}$. For Method C, the p and q values suggest second-order convergence of both α and $\tilde{x}$.

Having established convergence of our moving mesh schemes we now compare the numerical results from the methods of §4 with those of the method described in §3.

We generate results using the parameters detailed in (34) and (35). All three methods were investigated with $N = 80$, $\Delta t = 7.5 \times 10^{-3}$, and final time $t = 75$, i.e. 10,000 time-steps. Each of Methods A and C produce very similar results, so only the results from Method C and Method B are plotted below. Figures 9–11 are due to Method C and display the same travelling wave characteristics as the results in [1] for the same parameters (closely resembling Figures 1–3). The value of α near the free boundary remains fairly constant, and α at the centre of the tumour decreases at a steady rate as time increases. The velocity peaks near the boundary, but the velocity at the boundary appears to stay constant with respect to time for $t \geq 37.5$. This coincides with the tumour radius growing steadily, Figure 11. The minima are subtly different to that of [1]; the troughs in Figure 2, which resemble those in [1], are slightly less rounded than those shown in Figure 10. Interestingly, Method A (a locally conservative version of the method in §3) also presented rounder minima, identical to those in Figure 10.

Figures 12–14 show that Method B appears to behave like Method A and C (and [1]) at early times. However, after approximately $t = 45$, α appears to grow at the boundary, and no longer decreases at a regular rate at the centre of the tumour. Furthermore, the velocity at the boundary decreases considerably, with the tumour radius nearly reaching a steady state at $t = 75$. This behaviour is not apparent in [1], nor from Methods A and C. The plots from Method B are less

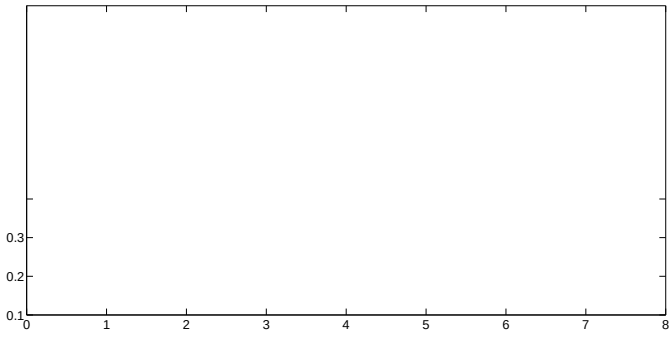
0.3
0.2
0.1
0
1
2
3
4
5
6
7
8

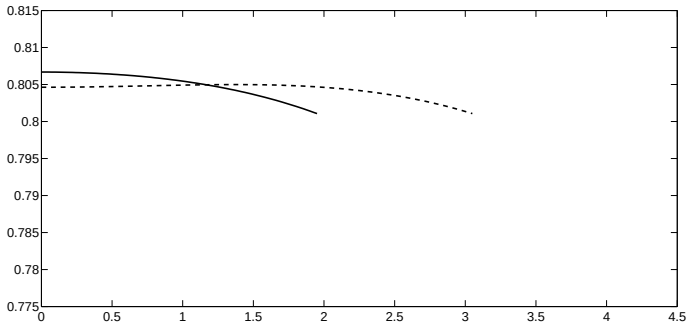
0.815
0.81
0.805
0.8
0.795
0.79
0.785
0.78
0.775
0
0.5
1
1.5
2
2.5
3
3.5
4
4.5

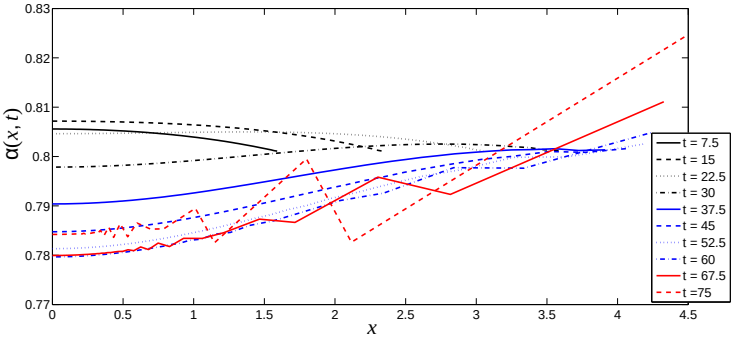

Figure 18: Cell volume fraction $\alpha(x, t)$ using Method B and parameter set (34) and (36).

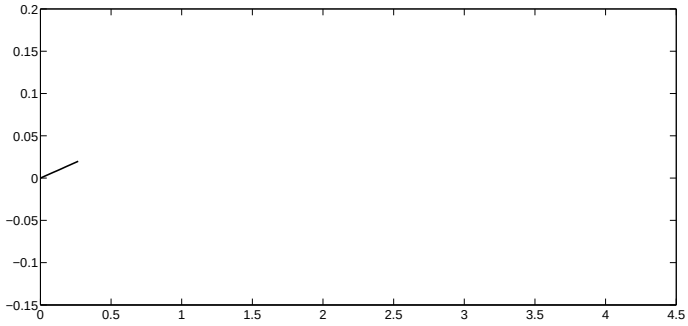

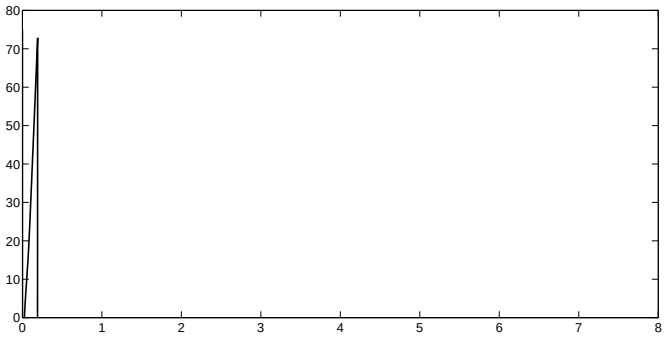
80
70
60
50
40
30
20
10
0
0
1
2
3
4
5
6
7
8

6. Conclusions

We have numerically solved the non-dimensionalised form of an avascular tumour growth model given in [1] using three different moving mesh methods. Working with the original non-dimensionalised form of the model, we have replicated the results of [1] and presented three different velocity-based approaches to move the mesh. The different approaches to define the

[10] Roose, T., Chapman, S. J. and Maini, P. K. (2007). Mathematical models of avascular tumour growth. *SIAM Rev.*, **49**, 179–208.
[11] Ward, J. P. and King, J. R (1997). Mathematical modelling of avascular tumour growth. *IMA J. Math. Appl. Med. Biol.*, **14**, 39–69.
[12] Please, C. P., Pettet, G. J. and McElwain, D. L. S. (1998). A new approach to modelling the formation of necrotic regions in tumours. *Appl. Math. Lett.*, **11**, 89–94.
[13] Please, C. P., Pettet, G. J. and McElwain, D. L. S (1999). Avascular tumour dynamics and necrosis. *Math. Models Methods Appl. Sci*, **9**, 569–579.
[14] Tindall, M. J. and Please, C. P. (2007). Modelling the Cell Cycle and Cell Movement in Multicellular Tumour Spheroids. *Bull. Math. Biol.*, **69**, 1147–1165.
[15] Byrne, H. M., King, J. R., McElwain, D. L. S and Preziosi, L. (2003). A two-phase model of solid tumour growth. *App. Math. Lett.*, **16**, 567–573.